RESEARCH OUTPUTS / RÉSULTATS DE RECHERCHE

In Plasma ion beam analysis of polymer layer and adsorbed H monolayer etching

Fortier, Louis Charles; Chicoine, Martin; Chouteau, Simon; Clausse, Mathilde; Lalande, Émile; Lussier, Alexandre W.; Roorda, Sjoerd; Stafford, Luc; Terwagne, Guy; Schiettekatte, François

In Plasma ion beam analysis of polymer layer and adsorbed H monolayer etching

Louis-Charles Fortier [a] , Martin Chicoine [a] , Simon Chouteau [a] , Mathilde Clausse [b] ,
Émile Lalande [a] , Alexandre W. Lussier [a] , Sjoerd Roorda [a] , Luc Stafford [a] , Guy Terwagne [b] ,
François Schiettekatte [a] ,*

[a] *Département de physique, Université de Montréal, C.P. 1628, succursale centre-ville, Montréal, H3C 3J7, Québec, Canada*
[b] *Université de Namur, rue de Bruxelles 61, Namur, B-5000, Belgium*

ARTICLE INFO

ABSTRACT

We present two experiments where a layer is plasma-etched while monitoring its evolution by *in plasma* ion beam analysis. First, we etch a photoresist with a diffuse O_2 plasma at low pressure. Using a 4.335 MeV He beam, Rutherford Backscattering Spectrometry and Elastic Recoil Detection spectra are acquired every minute during 8 h. Etching of most elements follows a linear trend, but H desorbs faster at the beginning of the plasma process, which we ascribe to the ion beam-induced desorption. In addition, we observe a thin Mo layer building up at the surface, likely due to the sputtering of an electrode in the plasma source. Secondly, we etch in HF a crystalline Si (c-Si) sample with $< 100 >$ surface orientation, which should leave 14 H/nm^2 bonded to the c-Si surface. The sample is then introduced in the chamber and exposed to a diffuse Ar plasma at low pressure. During plasma processing, the H surface concentration is monitored using a resonant nuclear reaction with a ^{15}N beam at 6.385 MeV. The initial H concentration is 11.7 ± 1.1 H/nm^2, and it decreases over a 3-minute timescale to an equilibrium concentration of 6.0 ± 0.8 H/nm^2. Over the range of experimental conditions investigated, the diffuse Ar plasma is therefore not able to entirely sputter the H from the c-Si surface.

1. Introduction

Ion beam analysis (IBA) and plasma treatments are generally understood as mutually exclusive as they operate in different pressure regimes. For example, the bias applied to a surface-barrier detector is sufficient to ignite a plasma in front of it, especially when a plasma is already present in the vacuum chamber. There are a few examples where IBA has been applied *in plasma*, revealing mechanisms that would otherwise be difficult to monitor. Examples include following the H+D content in graphite [1] or tungsten [2] exposed to the low-energy ion flux from a radiofrequency (RF) or direct-current (DC) deuterium plasma, monitoring the deposition and erosion of Li coatings submitted to plasma to simulate plasma-wall interactions in tokamaks [3], or the XeF_2 etching of Si [4]. In these examples, the particle detectors were protected, in the former case, by a foil of a few μm [5], and in the latter, because the experiment was conducted through a thin Si window. The backscattered particles, as well as the incident beam particles in the latter example, have to cross that amount of material, therefore they undergo energy straggling, which deteriorates the depth resolution. It also limits the application to materials that can be produced in thin layers and that can hold vacuum. Other similar examples of *in plasma* IBA and atmospheric pressure IBA are also found in the literature [6–8]. These experiments underline the significance of understanding the different plasma-surface mechanisms at play, as is also illustrated in the following Refs [9,10]. As highlighted in the Plasma Roadmap: low-temperature plasma science and technology [11,12], the use of *in situ* plasma-surface diagnostic tools will be a key enabler in the development of several plasma processes, including plasma-assisted atomic layer deposition [13,14] and etching [15,16] of thin films.

Here, we present plasma etching experiments monitored by *in plasma* Rutherford Backscattering Spectrometry (RBS, [17]) and other IBA techniques in a setup where differential pumping sections are used to bridge the pressure difference between the high vacuum of the accelerator tube and the RBS detector housing on the one hand, and the plasma chamber on the other.

The beam impinges the target at grazing incidence, optimizing the depth resolution near the sample surface. For H detection, the chamber is equipped with a standard absorber-foil Elastic Recoil Detection

---

system (ERD, [18]) and a γ detector for Nuclear Resonant Reaction Analysis with ^{15}N (NRRA, [19,20]).

We present two experiments to validate this approach. First, we carry out depth profiling while etching a photoresist with a diffuse O_2 plasma. Second, we perform surface analysis of a Si(100) sample saturated with adsorbed H while etching it with a diffuse Ar plasma.

2. Methodology

The setup, described in detail in Ref. [21], consists of a hemispherical chamber equipped with four plasma sources, all of which are oriented at 45° angle with respect to the target sample normal, and identified #1 through #4 in Fig. 1. For the purpose of this experiment, we used only the Inductively Coupled Plasma (ICP) source, #3, excited with RF at 13.56 MHz. This source is equipped with an inner Mo electrode that can be biased to accelerate the positive ions from the ICP source towards the outlet and thus, to produce a very-low-energy ion beam with a well-controlled average ion energy. In this work, the electrode was grounded such that its operation corresponds to the one of a conventional ICP source. The sample being located about 20 cm away, it is exposed to the diffuse region of the plasma source.

Additionally, the system is equipped with IBA detectors. To perform these measurements, the beam from a 1.7 MV Tandem accelerator crosses a differential pumping section and enters the chamber through a 1 mm circular aperture located 100 mm from the sample (#5 in Fig. 1), and impinges the target at an angle of 15° from the sample surface in order to increase the depth resolution. The RBS detector is located at the end of a cone (not shown) attached to the port #6 in Fig. 1 that limits gas conductivity. The pressure in the RBS detector section, which is attached to a separate turbo-molecular pump, is therefore one order of magnitude lower than in the main chamber, at a pressure where it can be biased without inducing a plasma in front of the detector. The sample-detector axis is at an exit angle of 45° of the sample surface and forms a scattering angle of 100.55° with the beam axis. The Elastic Recoil Detection (ERD) is located inside the port #7 in Fig. 1, which forms an angle of 30° with respect to the beam axis, and detects recoils at an angle of 15° from the surface. The slits (not shown) are located at the entrance of the port and are 5.00 ± 0.05 mm wide in the beam-detector axes plane. The size of the detector limits the solid angle in the other direction. A film of the appropriate thickness for each experiment (see below) blocks the port, both for absorbing the scattered beam ions and to prevent the gas or plasma from the main chamber to flow into the detector section. A γ detector is located right behind the sample holder, but in air, and separated from it by a thin Al window. This allows NRRA with a ^{15}N beam.

The first experiment consists in exposing a Si sample on which a photoresist is spin-coated. The photoresist's nominal composition is $H_{57}C_{28}O_{14}S_{0.5}$, but could be affected by residual amounts of solvent still in the film. A separate RBS measurement in another chamber, using a 3.06 MeV He beam to benefit from a nuclear resonance in O detection (not shown), yields the following stoichiometry: $H_{50\pm3}C_{42\pm4}O_{8\pm1}S_{0.5}$, somewhat off the nominal concentration, likely because of the presence of solvent residuals. A 4.35 MeV He beam is used to take advantage of a C nuclear resonance in the RBS spectrum [22]. This causes an increase in the amplitude of the C signal, making it clearly distinguishable from the Si substrate spectrum. However, this is at the expense of detecting O since no such enhanced cross-section occurs for that element at this beam energy, making the concentration of that element difficult to measure. During this experiment, the ERD slit is covered with 5.1 μm of Mylar as well as 10.5 μm of Al. A diffuse O_2 plasma at low pressure is used to etch the photoresist. The ICP source is operated at a power of 300 W and at a pressure of 5.7 ± 0.2 mTorr, with O_2 gas flowing at 15 sccm inside the source. The plasma source being at about 20 cm away from the sample, only a diffuse plasma reaches the surface [23]. In such conditions, the etching of the photoresist mostly results from the interaction with plasma-generated O atoms (mostly
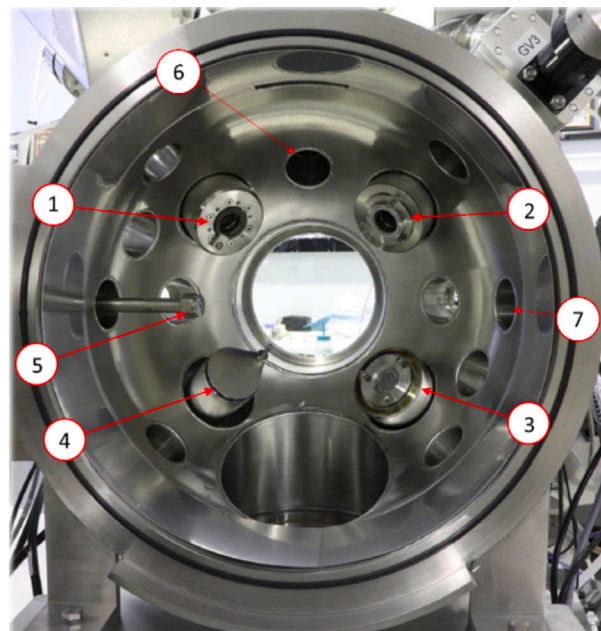

Fig. 1. Picture of the inside of the hemispherical chamber equipped with four plasma sources identified #1 through #4, source #3 being the one used for the experiments described in this paper. #5 is the entry path of the ion beam, while ports #6 and #7 respectively host the RBS and ERD detectors. All these instruments point towards a central location in front of the window, where the sample is located (not shown). The large port at the bottom is used for pumping.

chemical etching, leading to volatile CO_2), with a minor contribution from very-low-energy irradiation by O and O_2 positive ions [24,25]. After an initial etch of 4 h, the experiment was interrupted for an overnight break, and then the etching resumed for an additional 4 h.

For the second experiment, we first etch a crystalline Si sample with a (100) surface orientation in a 49% HF solution. Such etching removes the native oxide and leaves the Si (100) surface dangling bonds passivated with up to two H atoms per Si atom [26]. In less than 1 h, the sample is transported in atmospheric conditions and introduced in the chamber, which is then pumped down to very high vacuum. Such a short delay should result in minimal surface oxidation and loss of H [26]. A ^{15}N beam of 6.385 MeV is used to measure the H surface concentration. Collisions between ^{15}N ions at 6.385 MeV and stationary H atoms produce γ rays through a resonant nuclear reaction. These can be measured to quantify H concentration. Since this nuclear reaction can only occur within a few keV of its nominal value, considering the slowdown of the incident ions in the sample, this method provides measurements that are sensitive to a small depth interval [20]. During an initial measurement, the beam energy is scanned by a few keV to find the maximum γ ray yield. Then, a spectrum is acquired every minute, for 11 min, to observe potential beam-induced desorption effects, after which a diffuse Ar plasma at low pressure is turned on to etch the surface H from the Si(100) sample. During this time, the pressure is maintained at 2.0 ± 0.1 mTorr with Ar flowing into the source at 10 sccm, while 75 W of RF power is applied in the ICP source. In such conditions, etching of the hydrogenated Si surface can only result from very-low-energy irradiation by Ar positive ions, with possibly additional energy inputs by excited Ar neutrals and high-energy photons [27,28]. The γ yield is normalized to an H concentration with the help of an ERD spectrum acquired simultaneously. For these experiments, the entrance of the ERD detector is covered with 7.5 μm of Mylar. At the same time, an RBS spectrum is acquired every minute, and is used to quantify the flux of the incident beam.
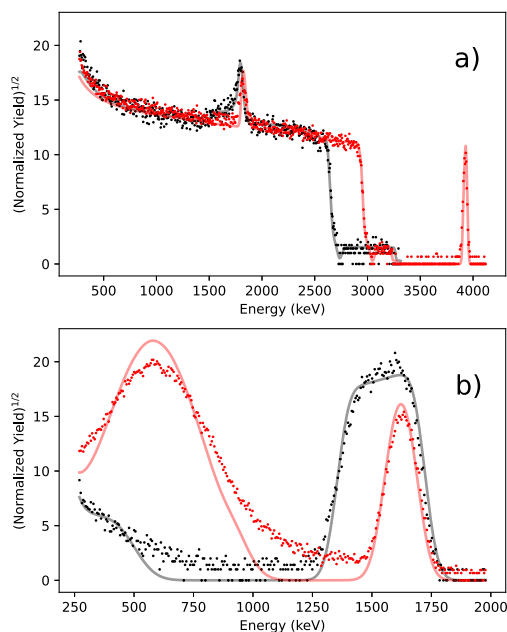
Fig. 2. (a) RBS and (b) ERD spectra before (black) and after (red) the photoresist plasma etching experiment. Both spectra present the square root of the yield to better observe some faint signals. The raw data is represented by the dots, while SIMNRA simulations are represented by the solid curves.

3. Results and discussion

3.1. Photoresist etching

Figures 2a and 2b respectively illustrate as dots the RBS and ERD spectra acquired during 15 min, without any plasma present, before the beginning (black) and after the end (red) of the etching experiment. In the RBS spectra, we see the C signal between 1500 and 1850 keV, on top of the Si substrate signal. The cross-section resonance happens in the top third of the as-deposited layer. Since all along the experiment, there is C at the top of the sample, this resonance peak is always present. However, the etching manifests itself by a receding low-energy edge of the C spectrum, which extends down to 1500 keV at the beginning, and shifts to 1700 keV at the end of the experiment. The S spectrum, which surface edge is at 3210 keV, extends to the edge of the Si substrate signal all along the experiment. The O signal, which should appear between 1950 and 2370 keV is not distinguishable. As mentioned, a separate RBS measurement before plasma etching allows us to find 11% O in the sample. Then, we observe that the Si signal edge shifts from 2660 to 2910 keV as a result of a decreasing amount of material on top of it.

We also note the emergence of a narrow Mo peak at 3930 keV, not visible at the beginning of the experiment. This indicates the presence of a growing Mo surface layer on the sample. We surmise that it results from the sputtering of the Mo electrode in the ICP source. Since this electrode was grounded in this work, the difference between the O_2 plasma potential and the Mo surface can accelerate ions in the sheath and induce sputtering of the Mo electrode. Mo atoms can then be transported by the Ar gas flow and condensate at the surface of the vacuum vessel, including the sample.

In Fig. 2b, the H peak initially extends from 1350 to 1640 keV (black), but becomes narrower (red) as the photoresist layer becomes thinner. We also note the presence of an important peak at low energy in the ERD spectrum acquired after the end of the etching experiment (red). It was not present before plasma etching (black). This peak results from He ions scattering on the Mo film, which then have enough energy to go through the absorber in front of the ERD detector. We can

use this peak to confirm the solid angle ratio between the RBS and ERD detector.

To extract the composition and areal density from these spectra, we perform SIMNRA simulations [29], fitting the composition of the sample to reproduce each RBS spectrum and the simultaneously acquired ERD spectrum. Such simulations are plotted as solid curves in Fig. 2 for both RBS (a) and ERD (b) measurements, acquired before (black) and after (red) the etching. We use these simulations to extract the ranges on which to integrate the peaks in the spectra acquired during the plasma etching experiment. We also use them to find the correspondence between the number of counts and the areal atomic density. The results are reported in Fig. 3. The peaks are normalized by the Si signal level to account for possible He beam intensity variations during etching.

In the case of C (blue squares), the relation between the integrated number of counts and the concentration is non-linear, as the resonance in the cross-section results in more counts for the top part of the layer. To establish this relation, we carry a series of SIMNRA simulations for different photoresist thicknesses between those from Fig. 2a, and integrate the simulated C peak from the simulation. This gives the relation between the C peak area (in counts) and the C areal density. The relation is then used to convert the C peak area from the spectra acquired in real-time during plasma etching to areal density as reported in Fig. 3. As for H and S, their areal densities are respectively plotted as green diamonds and cyan stars. The S data is multiplied by 30 for clarity. The total of the three areal densities (C, H, and S) is represented as red triangles. We can also deduce the total areal density from the shift of the Si substrate edge, from 2660 to 2910 keV, as mentioned previously. This is represented as black circles. The areal density and composition, before and after the etching, are reported in Table 1. The difference with the red triangles is consistent with the O content deduced separately. The vertical error bars are based on the counting statistics. The horizontal error bars simply indicate the time span on which spectra were summed, that is, 25 min.

We note in Fig. 3 that all elements are etched at an approximately linear pace, and their proportions remain the same, with the possible exception of the H, which features a slightly more rapid decrease in the first hour of the experiment. This last aspect is better illustrated in Fig. 4(a), which shows that the proportion of H in the layer goes from about 51% to about 39%. This can be explained by beam induced H desorption [30], noting that the He beam flux (gray curve, plotted against the right axis) was significantly higher during the first hour than in the rest of the plasma etching experiment. The variation in H content is small, however, so in addition to the vertical error bars, which are based on the counting statistics, the dashed line and the green band indicate the average H content and its standard deviation considering all the data covered by the dashed curve. This helps to confirm that the H content is slightly but significantly higher at the beginning of the plasma etching experiment.

In addition to the photoresist composition, we deduce from SIMNRA simulations of the RBS spectrum obtained after the etching experiment that a total of 230 ± 10 Mo/nm² is deposited at the surface of the layer. Assuming the bulk atom density of pure Mo, this corresponds to a thickness of 3.6 ± 0.2 nm. Fig. 4(b) shows the evolution of the Mo content as a function of time. It accumulates regularly but not as linearly as the etching in Fig. 3. The reason for that is not clear but might be linked to the exact conditions leading to the electrode erosion inside the ICP plasma source. For example, one may expect slight temporal variations of the Mo surface temperature due to neutral gas heating in the plasma source and subsequent heat transfer to plasma-exposed surfaces. We also see in Fig. 4(b) that the Mo accumulation rate changes near the overnight interruption of the plasma etching experiment (represented by the vertical dashed line in the figure). Although this was not investigated here, such metal condensation at the surface of an inert surface in the absence of an adhesion layer usually results in a discontinuous, nanostructured film [31], so it does
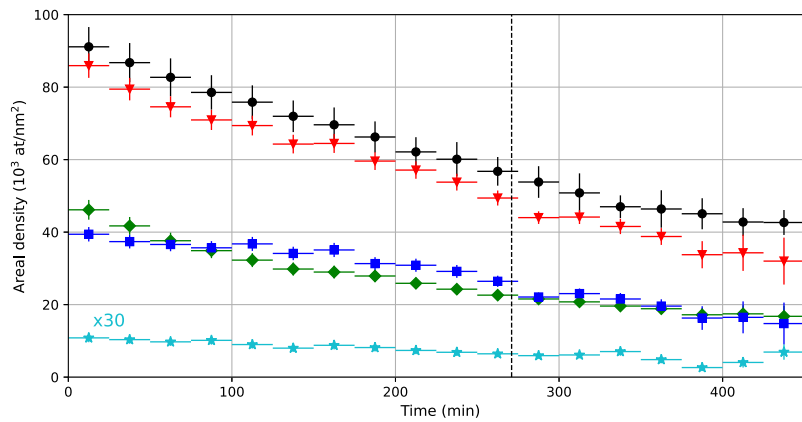
Fig. 3. Areal density of S (×30, cyan stars), C (blue squares), and H (green diamonds) as a function of plasma etching time. The red triangles correspond to the sum of the H, C and S areal densities, while the black circles represent the total areal density deduced from the shift in energy of the Si interface edge. The dotted line at t = 271 min corresponds to the overnight interruption in the experiment.

Table 1
Concentration of each element in the photoresist (first three lines) and areal atomic density (last two lines), before and after etching based on the data of Fig. 3.

Element	Before etching	After etching
H (%)	51 ± 3	40 ± 7
C (%)	43 ± 3	34 ± 14
S (%)	0.4 ± 0.05	0.6 ± 0.2
H+C+S (at/nm²)	86 000 ± 4000	32 000 ± 7000
from Si shift (at/nm²)	91 000 ± 6000	43 000 ± 4000

not prevent further etching or consumption of the C by the O_2 plasma. At least, we do not observe slowing etch rate corresponding to Mo progressively impairing the etch process.

In comparison with previous studies on polymers etching in low-pressure oxygen plasmas at room temperature [32,33], we note that the plasma etching of the photoresist is relatively slow, given that C should rapidly react with plasma-generated O to form highly volatile CO_2. The probable reason is that the plasma source is rather far from the target, and only a diffuse plasma reaches the surface. In such conditions, the populations of O atoms and positive ions (O and O_2) reaching the sample is relatively low, thus limiting the etching rate of the photoresist.

3.2. Surface hydrogen etching

This section examines the etching of the hydrogenated Si surface by the Ar plasma. As described in Section 2, the surface concentration is monitored simultaneously by RBS, ERD, and NRRA. Fig. 5(a) shows two γ ray spectra acquired during 1 min. The red data corresponds to the signal when the ^{15}N beam impinges the monolayer of H at the surface of the Si sample, with the beam energy optimized to yield the maximum signal. The black curve shows the background when a shutter is placed in front of the sample. The region between the channels 180 and 300 corresponds to the γ rays yield from the nuclear reaction: it is proportional to the H concentration at the surface. Fig. 5(b) represents the ERD spectrum accumulated during the entire experiment presented below. The red region corresponds to the surface H peak, while the background signal results from multiple collisions. The lower energy peak consist of beam ions that did cross the absorber foil.

The ratio of the ERD detector solid angle, $\Delta\Omega_{ERD}$, to that of the RBS detectors, $\Delta\Omega_{RBS}$, is known from separate measurements. The number of incident ions times the solid angle of the RBS detector, $q\Delta\Omega_{RBS}$, is known with precision from the simultaneously measured backscattering yield from the Si substrate, through a SIMNRA simulation. Knowing the solid angle ratio, this yields a similar factor, $q\Delta\Omega_{ERD}$, used to analyze
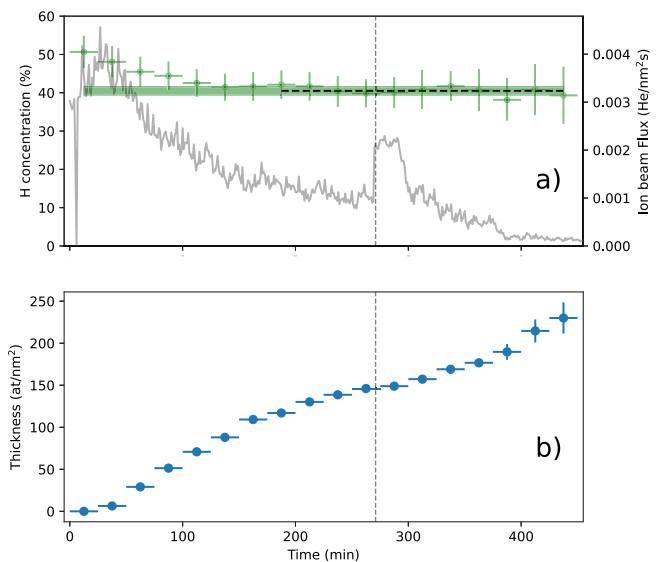

Fig. 4. (a) Proportion of H in the photoresist over the course of the etching (green dots, plotted against the left axis). The dashed line corresponds to the average of the data points it covers, while the green band corresponds to the standard deviation of the same points, extended over the entire time as a guide to the eye. The ion beam flux is plotted in gray and against the right axis. In both panels, the dotted vertical line indicates the overnight pause in the etching experiment. (b) Mo areal density at the surface of the photoresist as a function of time, deduced from the Mo peak area in the RBS spectra.

the ERD spectrum. We therefore know from the latter the total areal concentration of H measured over the whole experiment,

$$Nt_{H,tot} = \frac{n_{ERD}}{q\Delta\Omega_{ERD} \ (d\sigma/d\Omega)_{ERD}}, \tag{1}$$

where n_{ERD} is the area of the red peak in Fig. 5(b), and $(d\sigma/d\Omega)_{ERD}$ is the ERD differential cross section.

During the experiment, the H concentration can be deduced from the NRRA data using the following equation :

$$Nt_{H,i} = Nt_{H,tot} \frac{n_{NRRA,i}}{n_{NRRA,tot}} / \frac{n_{RBS,i}}{n_{RBS,tot}}, \tag{2}$$

where $n_{NRRA,i}/n_{NRRA,tot}$ corresponds to the ratio of γ ray yield during time step i of the etching experiment, to the yield over the complete experiment, and $n_{RBS,i}/n_{RBS,tot}$ is the same as for the RBS yield. The latter factor accounts for beam flux fluctuations.

The resulting calculations give us Fig. 6, that is, the H surface concentration as a function of time t_i. In this figure, the black triangles
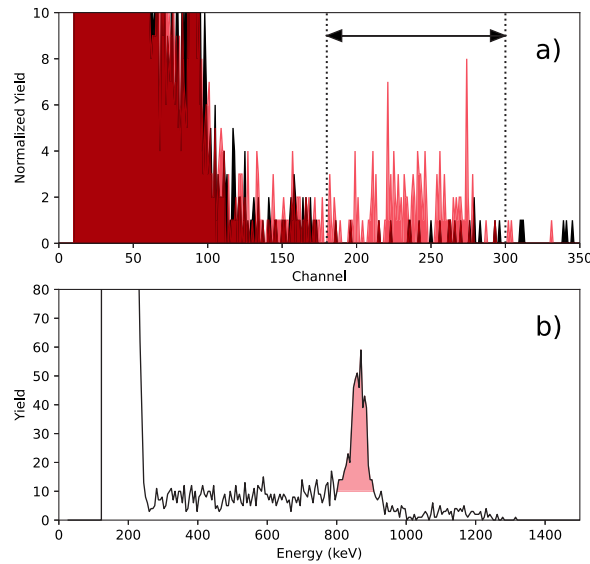
Fig. 5. (a) One minute-long acquisition on the γ-ray detector with the ^{15}N ion beam hitting the shutter (black) and the sample (red). (b) Time integrated ERD spectrum resulting from H recoiled by ^{15}N incident ions. The signal covering the first 50 channels corresponds to the ions that were not sufficiently slowed down by the foil. We identify an H surface peak denoted by the region highlighted in red.
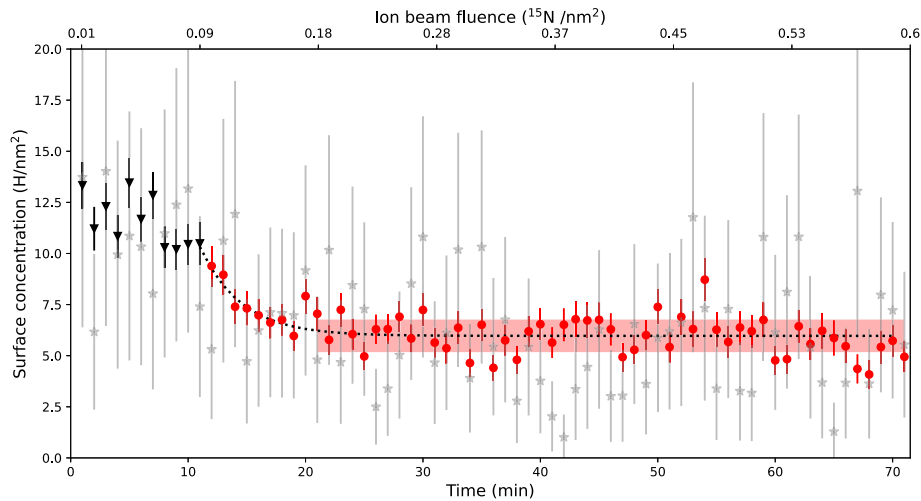

Fig. 6. Surface concentration of H on the Si sample. The black triangles represent the concentration measured by NRRA before the ignition of the plasma while the red dots denote those taken afterwards. The black dotted curve is Eq. (3) fitted on the data in red, where C_H corresponds to the average value of the region highlighted in red. The width of that band corresponds to the data standard deviation. The gray stars denote the H surface concentration measured by ERD.

represent the H concentration as measured by NRRA during a first phase, before the Ar plasma is turned on. The gray stars represent the H concentration as measured by ERD and suffer from poor counting statistics, so only the cumulative ERD measurement is of interest. We see from the trend in the black triangles that the ion beam induces some H desorption. We also observe that the initial concentration of H, 11.7 ± 1.1 H/nm^2, is slightly smaller than its nominal value of 14 H/nm^2. Such difference is expected given the 1-hour air exposure between the HF etch and the insertion of the Si sample in the chamber.

At $t_0 = 11$ minutes, the Ar plasma is turned on. That phase of the experiment is represented by the red dots. We see a sharp decrease in the H concentration, followed by a stabilization after about 10 min of plasma exposition, at $C_H = 6.0 \pm 0.8$ H/nm^2. The red band represents that average, taken over the range it covers, and its width corresponds to one standard deviation. We observe the same trend in the gray data set (ERD), but with significantly more statistical fluctuations as the number of counts is five times smaller compared to the NRRA yield. The dotted curve is a fit of the red data points by the following expression:

$$f(t) = Ae^{-(t-t_0)/\tau} + C_H, \tag{3}$$

which yields $A = 4.4 \pm 0.6$ H/nm^2 and $\tau = 3.5 \pm 0.4$ minutes.

The fact that the H surface concentration stabilizes at such a value is somewhat unexpected, given that plasma bombardment should remove most weakly-bond molecules from the Si surface. A possible explanation is the observation by Niwano et al. of the decrease of SiH$_2$ bonds in favor of the formation of SiH(O$_3$) over several hours during exposure of such surface to air [26]. This is consistent with our observation of the H concentration halving, but in a much-accelerated process. Over the range of experimental conditions investigated, the plasma source is located several centimeters away from the target such that the surface is only exposed to a diffuse plasma characterized by cold neutral Ar atoms and very low energy Ar ions and electrons. In such conditions, the mild plasma is most likely not able to entirely sputter the hydrogenated Si surface. Other mechanisms may also be at play to maintain a relatively constant surface H concentration.

These experiments underline the sensitivity of the *in plasma* NRRA measurements, as opposed to the ERD ones. Fig. 6 clearly shows that ERD measurements in this context are unable to, within their uncertainty, measure the plasma etching that took place. This reinforces the argument that ^{15}N NRRA is a more sensitive technique for surface hydrogen [20]. This holds true in a plasma for H adsorbed at the surface of a Si sample.

4. Conclusion

We have demonstrated that IBA measurements can be taken *in plasma*. We are able to quantify the total amount, relative proportion and etching rate of each element in a photoresist by an oxygen plasma, while monitoring undesired effects such as the accumulation of plasma-generated impurities. We also tracked and modeled the desorption of a single layer of surface H on a Si(100) sample *in plasma* and measured the characteristic etching rate by an Ar plasma. These experiments demonstrate the added value of *in plasma* IBA to study and better understand the physics and chemistry during plasma processing of materials.

Declaration of competing interest

Regarding the manuscript submitted, the authors have no Conflicts of Interest to declare.

Acknowledgments

References

[1] M. Langhoff, B.M.U. Scherzer, The hydrogen inventory in plasma exposed graphite surfaces, J. Nucl. Mater. 245 (1) (1997) 60–65, http://dx.doi.org/10.1016/S0022-3115(96)00746-5, URL https://www.sciencedirect.com/science/article/pii/S0022311596007465.

[2] M. Yamagiwa, Y. Nakamura, N. Matsunami, N. Ohno, S. Kajita, M. Takagi, M. Tokitani, S. Masuzaki, A. Sagara, K. Nishimura, In situmeasurement of hydrogen isotope retention using a high heat flux plasma generator with ion beam analysis, Phys. Scr. T145 (2011) 014032.

[3] F. Bedoya, K.B. Woller, D.G. Whyte, Study of the properties of thin Li films and their relationship with He plasmas using ion beam analysis in the DION-ISOS experiment, Rev. Sci. Instrum. 89 (10) (2018) 10J106, http://dx.doi.org/10.1063/1.5034240, arXiv:https://pubs.aip.org/aip/rsi/article-pdf/doi/10.1063/1.5034240/16732460/10j106_1_online.pdf.

[4] K.R. Padmanabhan, In situ ion beam analysis of chemical and plasma etching of Si, Modern Phys. Lett. B 15 (28n29) (2001) 1419–1427, http://dx.doi.org/10.1142/S0217984901003342.

[5] G.M. Wright, H.A. Barnard, L.A. Kesler, E.E. Peterson, P.W. Stahle, R.M. Sullivan, D.G. Whyte, K.B. Woller, An experiment on the dynamics of ion implantation and sputtering of surfaces, Rev. Sci. Instrum. 85 (2) (2014) 023503, http://dx.doi.org/10.1063/1.4861917, arXiv:https://pubs.aip.org/aip/rsi/article-pdf/doi/10.1063/1.4861917/13365244/023503_1_online.pdf.

[6] F. Schiettekatte, M. Chicoine, J. Forster, J. Geiger, S. Gujrathi, R. Kolarova, A. Paradis, S. Roorda, P. Wei, ERD, ^{15}N external beam for NRRA in air, HIRBS: Ion beam analysis developments on the HVEC EN-1 tandem, Nucl. Instrum. Methods Phys. Res. B 219–220 (2004) 430–434, http://dx.doi.org/10.1016/j.nimb.2004.01.096, URL https://www.sciencedirect.com/science/article/pii/S0168583X04001247, Proceedings of the Sixteenth International Conference on Ion Beam Analysis.

[7] L. Pichon, L. Beck, P. Walter, B. Moignard, T. Guillou, A new mapping acquisition and processing system for simultaneous PIXE-RBS analysis with external beam, Nucl. Instrum. Methods Phys. Res. B 268 (11) (2010) 2028–2033, http://dx.doi.org/10.1016/j.nimb.2010.02.124, URL https://www.sciencedirect.com/science/article/pii/S0168583X10002193.

[8] Z. Siketić, I. Bogdanović Radović, I. Sudić, M. Jakšić, Surface analysis and depth profiling using time-of-flight elastic recoil detection analysis with argon sputtering, Sci. Rep. 8 (1) (2018) 10392, http://dx.doi.org/10.1038/s41598-018-28726-x, URL https://www.nature.com/articles/s41598-018-28726-x, Publisher: Nature Publishing Group.

[9] K. Karahashi, S. Hamaguchi, Ion beam experiments for the study of plasma–surface interactions, J. Phys. D: Appl. Phys. 47 (22) (2014) 224008, http://dx.doi.org/10.1088/0022-3727/47/22/224008.

[10] M. Mayer, S. Möller, M. Rubel, A. Widdowson, S. Charisopoulos, T. Ahlgren, E. Alves, G. Apostolopoulos, N.P. Barradas, S. Donnelly, S. Fazinić, K. Heinola, O. Kakuee, H. Khodja, A. Kimura, A. Lagoyannis, M. Li, S. Markelj, M. Mudrinic, P. Petersson, I. Portnykh, D. Primetzhofer, P. Reichart, D. Ridikas, T. Silva, S.M.G.d. Vicente, Y.Q. Wang, Ion beam analysis of fusion plasma-facing materials and components: facilities and research challenges, Nucl. Fusion 60 (2) (2019) 025001, http://dx.doi.org/10.1088/1741-4326/ab5817, Publisher: IOP Publishing.

[11] I. Adamovich, S.D. Baalrud, A. Bogaerts, P.J. Bruggeman, M. Cappelli, V. Colombo, U. Czarnetzki, U. Ebert, J.G. Eden, P. Favia, D.B. Graves, S. Hamaguchi, G. Hieftje, M. Hori, I.D. Kaganovich, U. Kortshagen, M.J. Kushner, N.J. Mason, S. Mazouffre, S.M. Thagard, H.-R. Metelmann, A. Mizuno, E. Moreau, A.B. Murphy, B.A. Niemira, G.S. Oehrlein, Z.L. Petrovic, L.C. Pitchford, Y.-K. Pu, S. Rauf, O. Sakai, S. Samukawa, S. Starikovskaia, J. Tennyson, K. Terashima, M.M. Turner, M.C.M.v.d. Sanden, A. Vardelle, The 2017 plasma roadmap: Low temperature plasma science and technology, J. Phys. D: Appl. Phys. 50 (32) (2017) 323001, http://dx.doi.org/10.1088/1361-6463/aa76f5, Publisher: IOP Publishing.

[12] I. Adamovich, S. Agarwal, E. Ahedo, L.L. Alves, S. Baalrud, N. Babaeva, A. Bogaerts, A. Bourdon, P.J. Bruggeman, C. Canal, E.H. Choi, S. Coulombe, Z. Donkó, D.B. Graves, S. Hamaguchi, D. Hegemann, M. Hori, H.-H. Kim, G.M.W. Kroesen, M.J. Kushner, A. Laricchiuta, X. Li, T.E. Magin, S.M. Thagard, V. Miller, A.B. Murphy, G.S. Oehrlein, N. Puac, R.M. Sankaran, S. Samukawa, M. Shiratani, M. Šimek, N. Tarasenko, K. Terashima, E.T. Jr., J. Trieschmann, S. Tsikata, M.M. Turner, I.J.v.d. Walt, M.C.M.v.d. Sanden, T.v. Woedtke, The 2022 plasma roadmap: Low temperature plasma science and technology, J. Phys. D: Appl. Phys. 55 (37) (2022) 373001, http://dx.doi.org/10.1088/1361-6463/ac5e1c, Publisher: IOP Publishing.

[13] R.A. Ovanesyan, E.A. Filatova, S.D. Elliott, D.M. Hausmann, D.C. Smith, S. Agarwal, Atomic layer deposition of silicon-based dielectrics for semiconductor manufacturing: Current status and future outlook, J. Vacuum Sci. Technol. A 37 (6) (2019) 060904, http://dx.doi.org/10.1116/1.5113631.

[14] H.C.M. Knoops, T. Faraz, K. Arts, W.M.M.E. Kessels, Status and prospects of plasma-assisted atomic layer deposition, J. Vacuum Sci. Technol. A 37 (3) (2019) 030902, http://dx.doi.org/10.1116/1.5088582.

[15] K.J. Kanarik, T. Lill, E.A. Hudson, S. Sriraman, S. Tan, J. Marks, V. Vahedi, R.A. Gottscho, Overview of atomic layer etching in the semiconductor industry, J. Vacuum Sci. Technol. A 33 (2) (2015) 020802, http://dx.doi.org/10.1116/1.4913379.

[16] G.S. Oehrlein, D. Metzler, C. Li, Atomic layer etching at the tipping point: An overview, ECS J. Solid State Sci. Technol. 4 (6) (2015) N5041, http://dx.doi.org/10.1149/2.0061506jss, URL https://iopscience.iop.org/article/10.1149/2.0061506jss/meta, Publisher: IOP Publishing.

[17] W.-K. Chu, J.W. Mayer, M.-A. Nicolet, Backscattering Spectrometry, Academic Press, 1978, http://dx.doi.org/10.13140/RG.2.1.1948.0807.

[18] J. L'Ecuyer, C. Brassard, C. Cardinal, J. Chabbal, L. Deschênes, J.P. Labrie, B. Terreault, J.G. Martel, R. St.-Jacques, An accurate and sensitive method for the determination of the depth distribution of light elements in heavy materials, J. Appl. Phys. 47 (1) (1976) 381–382, http://dx.doi.org/10.1063/1.322288, arXiv:https://pubs.aip.org/aip/jap/article-pdf/47/1/381/18372375/381_1_online.pdf.

[19] W.A. Lanford, H.P. Trautvetter, J.F. Ziegler, J. Keller, New precision technique for measuring the concentration versus depth of hydrogen in solids, Appl. Phys. Lett. 28 (9) (1976) 566–568, http://dx.doi.org/10.1063/1.88826, arXiv:https://pubs.aip.org/aip/apl/article-pdf/28/9/566/18432824/566_1_online.pdf.

[20] M. Wilde, K. Fukutani, Hydrogen detection near surfaces and shallow interfaces with resonant nuclear reaction analysis, Surf. Sci. Rep. 69 (4) (2014) 196–295, http://dx.doi.org/10.1016/j.surfrep.2014.08.002, URL https://www.sciencedirect.com/science/article/pii/S0167572914000120.

[21] P. Vinchon, S. Asadollahi, C. Coté, S. Marcet, S. Atallah, E. Dessureault, M. Chicoine, A. Sarkissian, R. Leonelli, S. Roorda, F. Schiettekatte, L. Stafford, In-plasma analysis of plasma–surface interactions, Rev. Sci. Instrum. 94 (8) (2023) 083305, http://dx.doi.org/10.1063/5.0130235, arXiv:https://pubs.aip.org/aip/rsi/article-pdf/10.1063/5.0130235/18084673/083305_1_5.0130235.pdf.

[22] J.W. Bittner, R.D. Moffat, Elastic scattering of alpha particles by carbon, Phys. Rev. 96 (1954) 374–377, http://dx.doi.org/10.1103/PhysRev.96.374, URL https://link.aps.org/doi/10.1103/PhysRev.96.374.

[23] A. Granier, F. Nicolazo, C. Vallée, A. Goullet, G. Turban, B. Grolleau, Diagnostics in helicon plasmas for deposition, Plasma Sources Sci. Technol. 6 (2) (1997) 147, http://dx.doi.org/10.1088/0963-0252/6/2/008.

[24] O. Joubert, J. Pelletier, Y. Arnal, The etching of polymers in oxygen-based plasmas: A parametric study, J. Appl. Phys. 65 (12) (1989) 5096–5100, http://dx.doi.org/10.1063/1.343186.

[25] S.W. Pang, K.T. Sung, K.K. Ko, Etching of photoresist using oxygen plasma generated by a multipolar electron cyclotron resonance source, J. Vacuum Sci. Technol. B 10 (3) (1992) 1118–1123, http://dx.doi.org/10.1116/1.586087.

[26] M. Niwano, J.-i. Kageyama, K. Kurita, K. Kinashi, I. Takahashi, N. Miyamoto, Infrared spectroscopy study of initial stages of oxidation of hydrogen-terminated Si surfaces stored in air, J. Appl. Phys. 76 (4) (1994) 2157–2163, http://dx.doi.org/10.1063/1.357627, arXiv:https://pubs.aip.org/aip/jap/article-pdf/76/4/2157/8040360/2157_1_online.pdf.

[27] P. Vinchon, X. Glad, G. Robert-Bigras, R. Martel, A. Sarkissian, L. Stafford, A combination of plasma diagnostics and Raman spectroscopy to examine plasma-graphene interactions in low-pressure argon radiofrequency plasmas, J. Appl. Phys. 126 (23) (2019) 233302, http://dx.doi.org/10.1063/1.5125143.

[28] P. Vinchon, X. Glad, G.R. Bigras, A. Sarkissian, R. Martel, L. Stafford, Plasma–graphene interactions: Combined effects of positive ions, vacuum-ultraviolet photons, and metastable species, J. Phys. D: Appl. Phys. 54 (29) (2021) 295202, http://dx.doi.org/10.1088/1361-6463/abfe3b.

[29] M. Mayer, SIMNRA, a simulation program for the analysis of NRA, RBS and ERDA, AIP Conf. Proc. 475 (1) (1999) 541–544, http://dx.doi.org/10.1063/1.59188, arXiv:https://pubs.aip.org/aip/acp/article-pdf/475/1/541/12099238/541_1_online.pdf.

[30] F. Schiettekatte, G. Ross, A. Chevarier, N. Chevarier, A. Plantier, Ion beam induced depth profile modification of H, D and He implanted in Be, C and Si, Nucl. Instrum. Methods Phys. Res. B 132 (4) (1997) 607–619, http://dx.doi.org/10.1016/S0168-583X(97)00485-0, URL https://www.sciencedirect.com/science/article/pii/S0168583X97004850.

[31] M. Zhang, M.Y. Efremov, F. Schiettekatte, E.A. Olson, A.T. Kwan, S.L. Lai, T. Wisleder, J.E. Greene, L.H. Allen, Size-dependent melting point depression of nanostructures: Nanocalorimetric measurements, Phys. Rev. B 62 (2000) 10548–10557, http://dx.doi.org/10.1103/PhysRevB.62.10548, URL https://link.aps.org/doi/10.1103/PhysRevB.62.10548.

[32] L.P.T. Schepers, W.L. IJzerman, J. Beckers, Oxygen content dependent etch rate of single polymer microparticles confined in the sheath region of a low pressure radiofrequency argon/oxygen plasma, J. Phys. D: Appl. Phys. 51 (37) (2018) 375203, http://dx.doi.org/10.1088/1361-6463/aad5b4, Publisher: IOP Publishing.

[33] S. Saloum, S. Abou Shaker, M. Alwazzeh, R. Hussin, Polymer surface modification using He/O2 RF remote low-pressure plasma, Surf. Interface Anal. 53 (9) (2021) 754–761, http://dx.doi.org/10.1002/sia.6976, URL https://onlinelibrary.wiley.com/doi/abs/10.1002/sia.6976, _eprint: https://onlinelibrary.wiley.com/doi/pdf/10.1002/sia.6976.